Meccanica
https://doi.org/10.1007/s11012-024-01843-w

RESEARCH

# Computational modeling of cell motility and clusters formation in enzyme-sensitive hydrogels

**Pierfrancesco Gaziano · Michele Marino**

Received: 10 January 2024 / Accepted: 18 June 2024


**Abstract** In this paper, we propose an extension of a previous model of cell motility in tissue engineering applications recently developed by the authors. Achieving large-scale production of neo-tissue through biofabrication technologies remains challenging owing to the need of thoroughly optimizing all the relevant process variables, a task hardly attainable through solely trial and error approaches. Therefore, the present work is intended to provide a valid and effective computational-based support for neo-tissue formation, with a specific focus on the preliminary phase of such process, in which cells move through a polymeric scaffold (hydrogel) and then compact into clusters. Cell motility is modeled by resorting to the phase-field method, and by incorporating diffusion of nutrients from the external culture bath as well as the expression by cells of chemoattractant substances that bias the random path they otherwise would follow. The previous model has been enriched by additionally encompassing the secretion of enzymes by cells that cleave the crosslinks between the hydrogel polymer chains. As such, in the present model hydrogel degradation exhibits spatio-temporal variations in its chemo-physical properties related to the local amount of enzymes, which deeply affects cell motility. Numerical results showcase the pivotal importance of the cells micro-environment properties for their crawling in hydrogel scaffolds, opening towards the development of a predictive computational-aided optimization tool for neo-tissue growth in bioprinted scaffolds.

**Keywords** Tissue engineering · Cell motility · Phase-field model · Enzyme-sensitive hydrogels · Chemotaxis

## 1 Introduction

Biofabrication is a rapidly emerging multidisciplinary research field aimed at reproducing in laboratories functional tissues and organs faithfully mimicking, to a certain extent, the complexity of the native ones. Interest in this technology and its subsequent continuous development is mainly due to the impressive progress in the additive manufacturing technology (commonly known as 3D printing), which quickly made the equipment affordable and widespread [1]. This in turn has led to rapid advancements in the field of tissue engineering, particularly concerning applications in regenerative medicine (with the restoration of damaged or degenerated tissues) and in the food sector (e.g., cultivated meat) [2–5].

P. Gaziano (✉) · M. Marino
Department of Civil Engineering & Computer Science Engineering (DICII), University of Rome "Tor Vergata", Via del Politecnico 1, Rome 00133, Italy
e-mail: gaziano@ing.uniroma2.it

M. Marino
e-mail: m.marino@ing.uniroma2.it

Published online: 22 July 2024

The generation of tissue involves extracting a specific amount of stem or progenitor cells from various sources, and cultivating them in a culture medium to facilitate replication and differentiation. Tissue regeneration is easier if cells are enclosed in scaffolds, as they offer a biocompatible and mechanically supporting structure to which the cells can attach, grow and maintain their physiological functions [6, 7]. Among the various biomaterials, hydrogels have proved to be particularly suitable for this purpose, and are in fact the most employed ones, especially for soft tissue applications [8]. Hydrogels are polymers having a gel-like consistency and show the presence of physical or chemical crosslinks that bond together the polymeric chains. These increase viscosity and stiffness, and therefore are crucial to ensure the mechanical stability of the construct, enhancing its shape-fidelity and mechanical properties [9]. Besides, several studies have shown that hydrogels designed with crosslinks that are responsive to cell-secreted enzymes are promising platforms for tissue engineering better than their enzyme-insensitive counterparts [10–12]. In fact, enzyme-sensitive hydrogels create an environment that facilitates the deposition of extracellular matrix (ECM) and, more importantly, its elaboration (i.e. tissue growth), key aspects to create a macroscopic and optimized engineered tissue [13]. For such polymers, degradation occurs locally, as enzymes expressed by the encapsulated cells diffuse outward and cleave crosslinks in their neighborhood, creating space where ECM molecules can deposit [14]. The degradation kinetics of the hydrogel depend on the characteristics of the specific enzyme (such as size and kinetics), its local concentration, and the properties of the substrate, i.e. the initial density and type of crosslinks in the hydrogel. As a result, the diffusion–reaction mechanisms of cell-produced chemical species cause the crosslink density in enzyme-sensitive hydrogels to vary both over time and across different locations.

The initial stage of tissue development in hydrogel scaffolds involves the formation of cell clusters, which represent the precursors of tissue blocks. The amount of neotissue mass that can be produced in a given timeframe is closely tied to cell motility during this early phase. Cell movement within the scaffold depends on how growth factors, oxygen, nutrients and waste are transported through the construct, as well as by variations in the cells' local microenvironment that are related to hydrogel degradation and chemo-mechanical cues activated from neighboring cells [15]. Consequently, in enzyme-sensitive hydrogels, cell motility is strongly coupled with cellular chemo-biological mechanisms, as the diffusive-reactive properties of the secreted enzymes cause local variations over time in the hydrogel crosslink density and, consequently, in all of its chemo-physical properties. These changes, in turn, affect the timing of new cellular clusters formation.

In polymer environments, cell crawling results in a combination of random advances and rotations (known as persistent random motion), and a directed motion [16, 17]. This latter is primarily propelled by chemical and mechanical cues present in the extracellular environment, commonly referred to as chemotactic and durotactic stimuli, respectively [18, 19]. In chemotaxis, cells express specific signaling proteins serving as chemoattractants, leading to the accumulation of such molecules near the membranes of other cells and facilitating downstream signaling mechanisms for cell-cell communication (paracrine signaling). On the other hand, durotaxis consists in cell movement along gradients in substrate stiffness, which in this case represent the external cue.

Despite the undoubted advantages, the in vitro production of tissues still presents some challenges. Specifically, the optimization of both the quality and quantity of the final product necessitates a meticulous tuning of all the pertinent variables inherent in the process [20]. Therefore, a robust quantification and optimization of the pivotal experimental parameters is of crucial importance. However, due to the large number of variables characterizing the production process, each of which exhibits considerable variability in its optimal calibration across different scenarios, this task is rather challenging. Achieving such optimization through conventional trial-and-error methodologies is basically impractical, as the a-priori indeterminate nature of the tests leads to prolonged lead times and potentially prohibitive costs [21]. This circumstance significantly undermines the scalability of production and, consequently, compromises the practical utility of this methodology in real applications. A different strategy to tackle the problem is resorting to numerical models of cell motility and tissue growth, since they represent a fast and

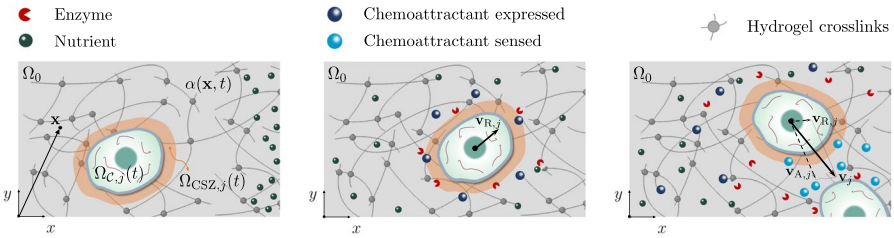


**Fig. 1** Rationale underlying the model of cell motility in an enzyme-sensitive hydrogel environment. All the symbols are introduced in the main text. The chemotactic sensing zone around the $j$-th cell ($\Omega_{CSZ,j}$) is highlighted in orange

cost-effective alternative to reproduce in silico many in vitro experiments [22, 23].

As such, this paper proposes an extension of the model of cell motility within hydrogel scaffolds presented by the authors in [24]. The dual nature of collective cell motion described earlier is encompassed, with a primary focus on chemotaxis as the principal driving force at the basis of directed motion. The process is modeled until the mutual adhesion between the cells and the consequent formation of a cluster occur. Consistently with our previous work, the moving boundary problem associated to cellular migration is mathematically approached via the phase-field (PF) methodology. This approach introduces a different scalar variable per cell (termed PF variable) to locate the evolving volume region occupied by each cell over time. The PF advective equations are coupled with other partial differential equations describing the most relevant mechanisms for the system evolution. Beyond the reaction/diffusion processes governing the chemoattractant molecules and nutrients dynamics (already included in [24]), the present study additionally incorporates the expression of enzymatic species by the cells, as well as their diffusion through the construct and their deactivation. Notably, this feature introduces a significant modification to the degradation mechanism of the hydrogel scaffold. In such scenario, the polymer crosslink density shows spatio-temporal variations as a consequence of a localized degradation due to a sufficient amount of enzyme concentration.

## 2 Materials and methods

In this Section, we illustrate the developed mathematical model of cellular motility. Our modeling philosophy is rooted in the premise of encompassing the most pertinent phenomena involved in this process, at the same time introducing the least possible amount of representative parameters, with the majority of them possessing a well-defined and precise physical meaning.

### 2.1 Modelling scenario and notation rules

Most of the features of the cell motility model previously developed by the authors in [24] are synthetically depicted in Fig. 1. Further information can be found in the original paper, to which interested readers are referred to. The model aims at describing the movement of cells starting from an initial configuration where a 3D printed filament of a cell-laden enzyme-degradable hydrogel is placed in a culture bath to stimulate the growth of neotissue. In this scenario, it is assumed that the cells will not proliferate nor increase in size, and that they receive nutrients diffusing through the construct from an external culture bath (not explicitly modelled). Nutrients are then consumed by the cells, and the energy produced by their metabolic processes is used for various purposes. We herein focus on the most significant cellular activities for the considered scenario, which include the generation of motion (linked to the polymerization of the actin network in the cytoskeleton), and the expression of both chemoattractant substances and enzymes. Enzymes diffuse through the hydrogel and cause a local disruption of the crosslinks, ushering the first phase of cell movement, characterized by a sequence of stochastic changes of polarization (persistent random motion). On the other hand, chemoattractants play the role of promoting intercellular communication (chemotactic paracrine signals), and therefore bias the random cell path by generating a motion directed towards similar cells. Ultimately, cells adhere to each other, forming clusters and thereby initiating the subsequent phase of tissue growth (not modelled within this framework). Note that in [24] the hydrogel degradation was only

attributed to an inherent natural reduction of the crosslink number over time, namely enzymatic-type degradation has not been taken into account.

Cell migration can be considered as a moving boundary problem (MBP), where the boundaries correspond to the cell membranes separating the intracellular region from the external hydrogel. The MBP addressed in the present model is tackled using a multi-phase-field method, in which a different scalar variable, defined over the (fixed) entire domain $\Omega_0$, is introduced for each cell. The $j$-th phase-field (PF) variable $\phi_j = \phi_j(\mathbf{x}, t)$ (with $j = 1, \dots, N_C$, where $N_C$ is the number of cells considered) is equal to 1 inside the volume region $\Omega_{C,j}(t)$ occupied at time $t$ by the $j$-th cell, and 0 outside. The variable $\phi_j$ displays a smooth transition between 0 and 1 across the interface, whose width depends on a regularization parameter $\varepsilon$. As such, it effectively acts as a marker to track over time the location of the cell. The definition of the $N_C$ PF variables allows the introduction of other phase-field-like variables serving as markers for the $j$-th cellular membrane ($\phi_{M,j}$), the extracellular hydrogel ($\phi_H$), as well as for the chemotactic sensing zone (CSZ) surrounding the $j$-th cell ($\phi_{CSZ,j}$):

$$\phi_{M,j} = A\,\phi_j^2(1-\phi_j)^2 \tag{1}$$

$$\phi_H = 1 - \phi = 1 - \sum_{j=1}^{N_C} \phi_j \tag{2}$$

$$\phi_{CSZ,j} = B^{C/2}\phi_j(1-\phi_j)^{2C}, \tag{3}$$

where $j = 1, \dots, N_C$, $\phi$ is defined through Eq. (2) and represents a cell-collective PF variable, and $A$, $B$, $C$ are positive constants.

For convenience, the following notation rules are introduced. For a generic, time-varying domain $\Omega_{\mathcal{D}}(t)$, the symbol $|\Omega_{\mathcal{D}}(t)|$ will denote its measure at time $t$, which in a diffuse-interface approach reads:

$$|\Omega_{\mathcal{D}}(t)| = \int_{\Omega_0} \phi_{\mathcal{D}}(\mathbf{x}, t)\, d\Omega, \tag{4}$$

$\phi_{\mathcal{D}}(\mathbf{x}, t)$ being the phase-field variable associated to the region $\Omega_{\mathcal{D}}$.[1] In particular, when $\Omega_{\mathcal{D}} \equiv \Omega_0$, it is assumed $\phi_{\mathcal{D}} = \phi_0 = 1$ in each point of $\Omega_0$. Given a vector-valued function $\mathbf{a}$, symbol $\langle \mathbf{a} \rangle_{CSZ,j}$ will denote its average value within the CSZ of the $j$-th cell, i.e.:

$$\langle \mathbf{a} \rangle_{CSZ,j} = \frac{1}{|\Omega_{CSZ,j}|} \int_{\Omega_{CSZ,j}} \phi_{CSZ,j}\, \mathbf{a}\, d\Omega. \tag{5}$$

Moreover, if $b$ is a scalar-valued function, the symbol $\mathcal{S}_+(b; b_0, \kappa_b)$ ($\mathcal{S}_-(b; b_0, \kappa_b)$, respectively) is used to synthetically denote an increasing (resp., decreasing) sigmoid function of $b$ between 0 and 1 dependent on the parameters $b_0$ and $\kappa_b$, namely:

$$\mathcal{S}_\pm(b; b_0, \kappa_b) = \frac{1 \pm \tanh\big(\kappa_b(b - b_0)\big)}{2}. \tag{6}$$

Specifically, $\kappa_b > 0$ regulates the steepness of the variation between 0 and 1, and $b_0$ is the sigmoid center, i.e. the value of $b$ for which $\mathcal{S}_\pm(b_0) = 1/2$. Lastly, symbol $E_s(b)$ will represent an exponential function of $b$ describing a saturation effect, i.e.:

$$E_s(b) = 1 - e^{-b/\tilde{n}}, \tag{7}$$

where $\tilde{n}$ is a fixed constant.

### 2.2 Mathematical model

The present model is based on the following main equations valid in $\Omega_0$:

$$\frac{\partial c_N}{\partial t} - \nabla \cdot (D_N \nabla c_N) = -\phi R_{MM} \tag{8}$$

$$\frac{\partial c_{S,j}}{\partial t} - \nabla \cdot (D_S \nabla c_{S,j}) = \phi_{M,j} P_{S,j} + Q_{S,j} \tag{9}$$

$$\frac{\partial \big(\phi_H \alpha\big)}{\partial t} = -\phi_H k_H\, c_E\, (\alpha - \alpha_\infty) \tag{10}$$

$$\frac{\partial \phi_j}{\partial t} + \mathbf{v}_j \cdot \nabla \phi_j = -\frac{1}{\eta\varepsilon} \frac{\delta \mathcal{H}_j}{\delta \phi_j} \tag{11}$$

Equations (8) and (9) represent diffusion–reaction equations for the nutrient, and for the chemical species S, which can be identified either with the chemoattractant molecule (S ≡ A) or the enzyme

[1] Note that, for simplicity, the symbol for the PF variable associated to the $j$-th cell is written as $\phi_j$ instead of $\phi_{C_j}$.

(S ≡ E). Symbols $c_N = c_N(\mathbf{x}, t)$, $c_{A,j} = c_{A,j}(\mathbf{x}, t)$ and $c_{E,j} = c_{E,j}(\mathbf{x}, t)$ denote the concentration fields of the nutrient, as well as of the chemoattractant and the enzyme produced by the $j$-th cell. The nutrient diffusion coefficient $D_N = D_N(\mathbf{x}, t)$ is defined by accounting for its variability in the intracellular ($D_{N,C}$) and hydrogel ($D_{N,H}$) domains as:

$$D_N = \phi\, D_{N,C} + \phi_H\, D_{N,H}. \tag{12}$$

Vice-versa, the enzyme and chemoattractant molecule can only diffuse in the extracellular environment, so their diffusivity is defined as: $D_S = D_S(\mathbf{x}, t) = \phi_H D_{S,H}$ (being S ≡ A or S ≡ E). In Eq. (8), the reaction term (right-hand side of the equation) is associated to cellular metabolic processes, described via the Michaelis-Menten kinetics:

$$R_{MM} = \frac{M_1 c_N}{M_2 + c_N}, \tag{13}$$

characterized by the constants $M_1$ and $M_2$. Note that the quantity:

$$R_j = \int_{\Omega_0} \phi_j R_{MM}\, d\Omega \tag{14}$$

represents the rate of nutrient metabolized by the $j$-th cell at time $t$. As such, this term is additively split into four contributions: $R_{A,j} = n_A R_j$, $R_{E,j} = n_E R_j$, $R_{v,j} = n_v R_j$, and $R_{O,j} = n_O R_j$, which are the nutrient rate consumption utilized by the $j$-th cell to express chemoattractant ($R_{A,j}$), to produce the enzyme ($R_{E,j}$), to generate motion ($R_{v,j}$), and to accomplish other processes linked to cellular metabolism ($R_{O,j}$), respectively. The coefficients $n_A$, $n_E$, $n_v$ and $n_O$ all range between 0 and 1, and are such that $n_A + n_E + n_v + n_O = 1$.

On the other hand, the reaction terms for the chemoattractant and the enzyme are source terms, as these molecules are produced at the level of the cellular membrane with a rate $P_{S,j}$ expressed as:

$$P_{S,j} = P_S^{\infty} E_s(R_{S,j}), \qquad S \in \{A,E\}. \tag{15}$$

The previous equation describes a saturation effect for the production of both chemoattractant and enzyme up to an asymptotic level $P_S^{\infty}$. Moreover, in Eq. (9) a term accounting for the natural decay of both chemoattractant and enzyme has been included and assumed in the form: $Q_{S,j} = -q_S c_S$, with S ∈ {A,E}.

Equation (10) describes the evolution in time of the crosslink local density degree $\alpha = \alpha(\mathbf{x}, t)$, a dimensionless variable representing the ratio between the crosslink density at position $\mathbf{x}$ and time $t$ and its maximum (i.e., initial) value. Hence, $\alpha \in [\alpha_{RG}, 1]$, where $\alpha_{RG}$ is the point of reverse gelation, i.e. the value of $\alpha$ for which the hydrogel melts. The parameter $k_H$ is dependent on the hydrogel composition, as it is related to the half-life time constant [25]. Note that a major difference with respect our previous model is the coupling between the decay in the hydrogel crosslink density and the total local concentration of the enzyme $c_E = \sum_{j=1}^{N_C} c_{E,j}$.

Equation (11) is a modified version of the classical Allen-Cahn equation, and describes the motion of the $j$-th cell as dependent on a drag coefficient $\eta$, a membrane active velocity $\mathbf{v}_j$, and on a Hamiltonian $\mathcal{H}_j$. The Hamiltonian represents the energy functional associated with the membrane and can be defined in different manners according to the most relevant phenomena involved in the process. In this work, we have considered the following form for $\mathcal{H}_j$:

$$\mathcal{H}_j = \mathcal{H}_{\phi_j} + \sum_{h \neq j}^{N_C} \mathcal{H}_{int,h}, \tag{16}$$

where $\mathcal{H}_{\phi_j}$ is the Hamiltonian for the single $j$-th cell, and $\mathcal{H}_{int,h}$ is the energy arising from its interaction with the $h$-th cell. The former contribution is given by [26]:

$$\mathcal{H}_{\phi_j} = \int_{\Omega_0} \left[ \gamma \left( \frac{G(\phi_j)}{\varepsilon} + \frac{\varepsilon}{2} \left\| \nabla \phi_j \right\|^2 \right) + \frac{\kappa}{2} \left( \frac{|\Omega_{\mathcal{C},j}(0)|}{|\Omega_0|} - \phi_j \right)^2 \right] d\Omega. \tag{17}$$

In Eq. (17), $\gamma$ is the surface tension, $\kappa$ is a penalty multiplier enforcing volume conservation for the cells, and $G(\phi_j) = m\,\phi_j^2(1 - \phi_j^2)$ is a double-well potential which, having local minima in 0 and 1, ensures the stable coexistence of both cell and hydrogel domains. The constant $m$ represents the maximum value of the double-well potential, and determines the strength with which $G$ constrains the interface thickness to have a finite size. On the other hand, the cell-cell interaction energy functional accounts for the repulsion between the interiors of

two cells, and the adhesion between the cell membranes [27, 28]:

$$\mathcal{H}_{\text{int},h} = \int_{\Omega_0} \left( \frac{\zeta}{2} \phi_j^2 \phi_h^2 + \frac{\sigma \varepsilon^3}{4} \|\nabla \phi_j\|^2 \|\nabla \phi_h\|^2 \right) d\Omega, \tag{18}$$

$\zeta$ and $\sigma$ being two positive parameters penalizing cell-cell overlapping and controlling the adhesion energy between the cellular membranes, respectively. Note that, with respect to our previous study, we included in the Hamiltonian the $\zeta$-term, and that all phase-field parameters have been recast so as to have a more clear physical meaning.

Analogously to [24] (to which reference has to be made for more details), the total velocity of the $j$-th cell, $\mathbf{v}_j$, is defined as:

$$\mathbf{v}_j = f_{\text{H}}(\bar{\alpha}_j)\, E_{\text{s}}(R_{\text{v},j})\, (\mathbf{v}_{\text{R},j} + \mathbf{v}_{\text{A},j}). \tag{19}$$

In Eq. (19) $\mathbf{v}_{\text{A},j}$ represents the chemotaxis-driven velocity component of the $j$-th cell. This is assumed to be proportional, according to a constant $k_{\text{A}}$, to the average value of the total gradient of chemoattractant concentration sensed within the $j$-th CSZ:

$$\mathbf{v}_{\text{A},j} = k_{\text{A}} \bar{\mathbf{g}}_{\text{A},j} = k_{\text{A}} \left\langle \sum_{h \neq j}^{N_{\text{C}}} \nabla c_{\text{A},h} \right\rangle_{\text{CSZ},j}. \tag{20}$$

On the other hand, $\mathbf{v}_{\text{R},j}$ is the random velocity component, given in the form of a rigid roto-translation around the cell's centroid. Its magnitude $v_{\text{R},j} = \left\| \mathbf{v}_{\text{R},j} \right\|$ is defined accounting for the gradual switch of the cell's motion from a random regime to a chemotactic-driven one, as follows:

$$v_{\text{R},j} = v^{\infty} \mathcal{S}_{-}(\|\bar{\mathbf{g}}_{\text{A},j}\|; g_{\text{A}}^{*}, \kappa_g) \tag{21}$$

Indeed, when a sufficiently high amount of total chemoattractant concentration gradient ($\|\bar{\mathbf{g}}_{\text{A},j}\| > g_{\text{A}}^{*}$) is sensed within the $j$-th CSZ, the magnitude of the random velocity component in Eq. (21) gradually decreases up to a null value, the steepness of such a transition being regulated by the positive constant $\kappa_g$. The randomness of the velocity component $\mathbf{v}_{\text{R},j}$ is given by both the time interval between two successive reorientations $\tau_{\text{R}}$ (which follow an exponential probability distribution) and the entity of such reorientations (characterized by a Gaussian statistics with null mean value and standard deviation $\sigma_{\text{R}}$). Hence, each cell independently follows a random piecewise-linear path until a high enough value of chemoattractant gradient is sensed within its CSZ. Lastly, the multiplying factors $f_{\text{H}}$ and $E_{\text{s}}$ in Eq. (19) make explicit the dependency of the total cell velocity upon the rate of nutrient employed by the cell to generate motion $R_{\text{v},j}$, and the average crosslink density $\bar{\alpha}_j(t) = \langle \phi_{\text{H}} \alpha \rangle_{\text{CSZ},j}$ of the hydrogel in the cell neighborhood. In particular, cell motion is hindered for too much high or low values of the hydrogel crosslink density, and we described this phenomenon by postulating the subsequent expression for the crosslink density-related velocity-bias function $f_{\text{H}}$:

$$f_{\text{H}}(\bar{\alpha}_j) = f_{\max} \min \left\{ \mathcal{S}_{+}(\bar{\alpha}_j; \alpha_{\text{RG}}, \kappa_\alpha); \mathcal{S}_{-}(\bar{\alpha}_j; \alpha_{\text{MO}}, \kappa_\alpha) \right\}, \tag{22}$$

where $f_{\max}$ is a constant related to the hydrogel chemo-physical properties, $\alpha_{\text{MO}}$ is the upper-threshold value of $\alpha$ for which cell motion can occur in the hydrogel, and the parameter $\kappa_\alpha > 0$ controls the steepness of the sigmoids $\mathcal{S}_{+}$ and $\mathcal{S}_{-}$ between 0 and 1.

### 2.3 Numerical implementation

The resulting set of coupled differential equations Eqs. (8)-(11) are discretized in time via a Backward Euler finite difference scheme, and in space through the finite element (FE) method. As in our previous work, this study exclusively addresses two-dimensional applications. Hence, all volumetric physical quantities have to be regarded as per unit thickness. A customized quadrilateral FE with bi-linear shape functions (henceforth referred to as Q1PF element) has been implemented through a hybrid simbolic-numeric strategy by exploiting the AceGen package of Wolfram Mathematica environment (v. 13.1). The nodal variables $\mathbf{p}$ are represented by the $N_{\text{C}}$ PF variables and the concentration fields of the mobile species (nutrient, chemoattractants, enzymes). On the other hand, the hydrogel crosslink density degree $\alpha$ has been treated as a history variable stored at the Gauss point level.

In the framework of variational formulations and following a well-established procedure (see e.g., [29]), the weak form associated to the governing equations can be obtained by imposing the stationarity condition of a pseudo-potential $\Pi$, reported in the Appendix A for the sake of

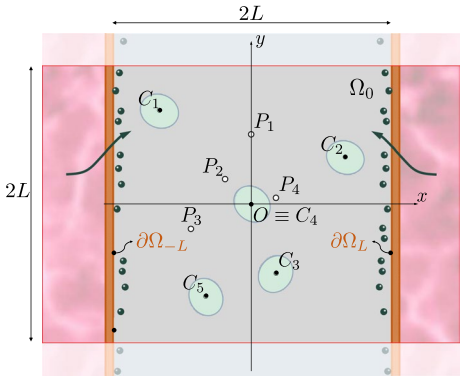


**Fig. 2** Sketch illustrating the set-up of numerical simulations: geometry of the domain, cells initial shape and centroid positions ($j = 1, \dots, 5$), points $P_k$ ($k = 1, \dots, 4$) in which the hydrogel crosslink density over time is probed

completeness. By inserting the FE discretization, the element-wise residual vector $\mathbf{R}$ thus results:

$$\mathbf{R}(\mathbf{p}) = \frac{d\Pi(\mathbf{p})}{d\mathbf{p}}\bigg|_{\mathbf{B}=\text{const.}}, \tag{23}$$

where $\mathbf{B}$ is a vector collecting quantities involved in differentiation exceptions for the consistent derivation of the residual form $\Pi$. These are also specified in Appendix A.

Lastly, the element-wise tangent matrix $\mathbf{K}$ is obtained by computing the derivative of $\mathbf{R}$ with respect to the nodal variables:

$$\mathbf{K} = \frac{d\mathbf{R}}{d\mathbf{p}}. \tag{24}$$

## 3 Results

The model is employed to simulate the motion of $N_C = 5$ cells within a 2D square domain $\Omega_0$ with sides of length $2L = 120\,\mu\text{m}$ (see Fig. 2), which stands for a representative region within a long filament of a tissue engineering construct [43]. Exact initial positions of cells centroids and cells' initial polarization are reported in Table 1, together with the coordinates of four randomly selected points $P_k$ to probe the temporal variation of the local hydrogel crosslink density. The enzyme-sensitive hydrogel has an initial homogeneous crosslink density degree equal to the unity everywhere in the extracellular environment. After a preliminary convergence analysis, the domain $\Omega_0$ has been discretized through Q1PF elements with mesh size equal to $0.5\,\mu\text{m}$, while a maximum time step equal to 2 min has been adopted.[2] Values of chemo-biological parameters are given in Table 2, where also the chemo-physical quantities characterizing the enzyme-sensitive hydrogel are listed. Finally, Table 3 reports values of the PF- and velocity-related model parameters. A thorough and extensive discussion of all the adopted values can be found in [24].

**Table 1** Values of cells initial centroids position $C_j$ ($j = 1, \dots, 5$), cells initial orientation angles with respect to the $x$-axis, and coordinates of the points $P_k$ ($k = 1, \dots, 4$) shown in Fig. 2

| Point | $x$-coordinate | $y$-coordinate | Orientation |
|---|---|---|---|
| *Cells initial positions and polarizations* | | | |
| $C_1$ | $-2/3L$ | $2/3L$ | $-30°$ |
| $C_2$ | $2/3L$ | $1/3L$ | $-25°$ |
| $C_3$ | $1/6L$ | $-1/2L$ | $60°$ |
| $C_4$ | 0 | 0 | $130°$ |
| $C_5$ | $-1/3L$ | $-2/3L$ | $110°$ |
| *Probe points* | | | |
| $P_1$ | 0 | $1/2L$ | – |
| $P_2$ | $-1/6L$ | $1/6L$ | – |
| $P_3$ | $-5/12L$ | $-1/6L$ | – |
| $P_4$ | $1/6L$ | $1/12L$ | – |

### 3.1 Boundary and initial conditions

At time $t = 0$, all cells are both positioned and polarized randomly in $\Omega_0$, and have an elliptical shape with major and minor semi-axes equal to $7\,\mu\text{m}$ and $6\,\mu\text{m}$, respectively. The domains $\Omega_{C,j}$ are initially located by imposing smooth sigmoid-type initial conditions for the $N_C$ PF variables $\phi_j$ in $\Omega_0$.

To replicate a typical experiment in which the cell-laden filament is immersed in a culture bath having volume $V_b = 2|\Omega_0|$ (pink-colored domain in Fig. 2, not explicitly modelled), nutrients are assumed to diffuse only through the lateral boundaries of $\Omega_0$, $\partial\tilde{\Omega} \equiv \partial\Omega_{-L} \cup \partial\Omega_L$. Nutrient concentration on $\partial\tilde{\Omega}$, $\tilde{c}_N$,

[2] Note that we implemented the same adaptive time stepping numerical strategy as in our previous work. For further details, the reader is therefore referred to [24].

**Table 2** Values of model parameters of the diffusing chemical species (nutrient, enzyme, chemoattractant) and the hydrogel scaffold

| Parameter | Symbol | Value | Unit | Source |
|---|---|---|---|---|
| *Nutrient (Glucose)* | | | | |
| Diffusivity through hydrogel | $D_{N,H}$ | 230 | $\mu m^2/s$ | [30, 31] |
| Diffusivity through cells | $D_{N,C}$ | 84 | $\mu m^2/s$ | [32] |
| Maximum consumption rate | $M_1$ | $2.45 \times 10^{-4}$ | mM/s | [33] |
| Half-maximum consumption | $M_2$ | $6 \times 10^{-3}$ | mM | [34, 35] |
| Fraction consumed for velocity | $n_v$ | 0.40 | – | Assumed |
| Fraction consumed for chemoattractant | $n_A$ | 0.25 | – | Assumed |
| Fraction consumed for enzyme | $n_E$ | 0.25 | – | Assumed |
| *Chemoattractant (Interleukin-6)* | | | | |
| Diffusivity (through hydrogel) | $D_{A,H}$ | 27 | $\mu m^2/s$ | [36] |
| Maximal production rate | $P_A^\infty$ | 18.5 | pM/s | [37] |
| Degradation rate | $q_A$ | 1.0 | 1/s | [24] |
| Constant for the saturation factor $E_s$ | $\tilde{n}$ | 1.7 | fmol/d | [38] |
| *Enzyme (Trypsin)* | | | | |
| Diffusivity (through hydrogel) | $D_{E,H}$ | 29 | $\mu m^2/s$ | [9] |
| Maximal production rate | $P_E^\infty$ | 2.3 | fM/s | [13] |
| Degradation rate | $q_E$ | 0.72 | 1/d | [13] |
| *Hydrogel scaffold (PEG-fibrinogen)* | | | | |
| Time-degradation constant | $k_H$ | 0.74 | 1/(M min) | Fitted from [9] |
| Regime crosslink density | $\alpha_\infty$ | 0.497 | – | Fitted from [9] |
| Steepness of velocity bias function | $\kappa_\alpha$ | 25 | – | [24] |
| Maximal velocity fraction | $f_{max}$ | 0.64 | – | [9] |
| Maximal crosslink degree for mobility | $\alpha_{MO}$ | 0.90 | – | [9] |
| Crosslink degree for reverse gelation | $\alpha_{RG}$ | 0.32 | – | [39] |

**Table 3** Values of the phase-field- and velocity-related model parameters

| Parameter | Symbol | Value | Unit | Source |
|---|---|---|---|---|
| *Phase-field* | | | | |
| Drag coefficient | $\eta$ | 31 | $nNs/\mu m^2$ | [40] |
| Interfacial length scale | $\varepsilon$ | 1.0 | $\mu m$ | [41] |
| Strength of double-well potential | $m$ | 18 | – | [24, 26] |
| Surface tension | $\gamma$ | 2.0 | pN | [28] |
| Volume penalty multiplier | $\kappa$ | 17.8 | $nN/\mu m^3$ | Estimated |
| Strength of cell-cell repulsion | $\zeta$ | 0.5 | $pN/\mu m$ | [26] |
| Adhesion energy parameter | $\sigma$ | 0.19 | pN | [28] |
| Membrane coefficient | $A$ | 16 | – | [24] |
| First CSZ coefficient | $B$ | 2 | – | [24] |
| Second CSZ coefficient | $C$ | 40 | – | [24] |
| *Velocity* | | | | |
| Time between reorientations | $\tau_R$ | 8 | min | [42] |
| Standard deviation of reorientations | $\sigma_R$ | 0.20 | rad | [42] |
| Maximal cell velocity | $v^\infty$ | 30 | $\mu m/h$ | [38] |
| Chemotactic constant | $k_A$ | 6 | $\mu m^2/$ (nM s) | [24] |
| Critical chemoattractant gradient | $g_A^*$ | 40 | $fM/\mu m$ | [24] |
| Steepness of random velocity function | $\kappa_g$ | 10 | $\mu m/pM$ | [24] |

is supposed to decrease over time as a consequence of the progressive nutrient depletion in the culture bath, according to the following mass balance:

$$V_b \tilde{c}_N(t) = V_b \tilde{c}_N(0) - m_N(t). \tag{25}$$

Equation (25) prescribes that, by assuming in the culture bath a homogeneous nutrient concentration equal to $\tilde{c}_N(t)$ at every time instant, the current nutrient mass in the culture medium is equal to the initial one diminished by the total mass $m_N(t)$ of nutrient consumed up to time $t$ by all cells, computable as follows:

$$m_N(t) = \int_0^t \sum_{j=1}^{N_C} R_j \, dt. \tag{26}$$

Furthermore, a stiffer outer shell providing stability to the construct and offering a topological guidance to cells (i.e., preventing they exit from the lateral boundaries $\partial\tilde{\Omega}$) has additionally been considered [43, 44]. In particular, it is assumed that cells invert their motion when they detect in their CSZ the lateral boundaries. Lastly, no flux conditions for all the primal variables are imposed on the upper/lower boundaries of $\Omega_0$.

### 3.2 Cell motion in enzyme-sensitive hydrogels

In this Section we present numerical results obtained from the case study detailed in Sect. 3.1, demonstrating the model's effectiveness in replicating the main chemo-biological mechanisms orchestrating cellular motility within enzyme-sensitive hydrogels, as well as their compaction in clusters.

To emphasize that the hydrogel degradation is induced by the local total concentration of cell-secreted enzymes, Fig. 3 reports snapshots of the crosslink density variable $\alpha$ at times $t = 2.5, 5, 7.5, 10\,\text{h}$. Recalling that the minimum value for $\alpha$ is the point of reverse gelation $\alpha_{RG}$, as a consequence of Eq. (10), the domain instantly occupied by the cell can be identified as the regions with $\alpha \simeq 0$, that are highlighted in white color in Fig 3. In the panels, the trajectory of each cell's centroid up to the corresponding time is additionally shown. In a first phase, all cells are blocked in their respective initial positions, due to the excessively high value of the hydrogel crosslink density. When cells start producing enzymes, these diffuse and accumulate in the cells neighborhood, causing the gradual degradation of the surrounding polymer. Hence, as soon as the average value of $\alpha$ in the CSZ of cells reaches the value $\alpha_{MO}$, cell motion can start. The cells then move through the hydrogel by "digging tunnels" stemming from the local cleavage of crosslinks due to the secreted enzymes, up to the moment of mutual adhesion, thus forming a cellular cluster. It is worth noting that the cell paths traced in the panels clearly illustrate the switch from a random to a chemotactic motion regime, as cells starts chasing one another when they are sufficiently close. Note also the slight modification of the cell's shape in the final part of the process (lower panels in Fig. 3), which is caused by the energy terms associated to adhesion and repulsion between the intracellular regions. Furthermore, it can be observed that the model correctly captures the barrier effect induced by the outer stiffer shell, which tends to divert the cells when trying to exit from the lateral boundaries. For the present case study, this is experienced by the cell whose centroid's path is marked in red color in the panels in Fig. 3. It is important to remark that the model is able to predict the typical timespan of formation of the early cellular clusters, available e.g. in the experiments performed by Eigler and coworkers [45].

Upon cellular aggregation, diverse topological configurations of clusters in terms of levels of compactness may arise. In fact, this is a key aspect for the efficacy of the successive phase of neo-tissue formation. With the aim of providing quantitative information regarding the compactness of forming clusters, we have defined in [24] the dimensionless Packing Index (PI) as follows:

$$\text{PI}(t) = \frac{H_0 - H(t)}{H_0 - H_{\min}} \tag{27}$$

where $H(t)$ is the area of the convex hull of the cells (herein identified as the set of all points such that $\phi \geq 0.5$) at time $t$, $H_0 = H(0)$ is its initial value, and $H_{\min}$ corresponds to the value of the PI in the configuration in which all cells are equal ellipses arranged according to a hexagonal lattice. The plot over time of the PI for the present case study is reported in Fig. 4, and it is compared to a PI curve obtained from our previous study [24]. For the present scenario, the PI

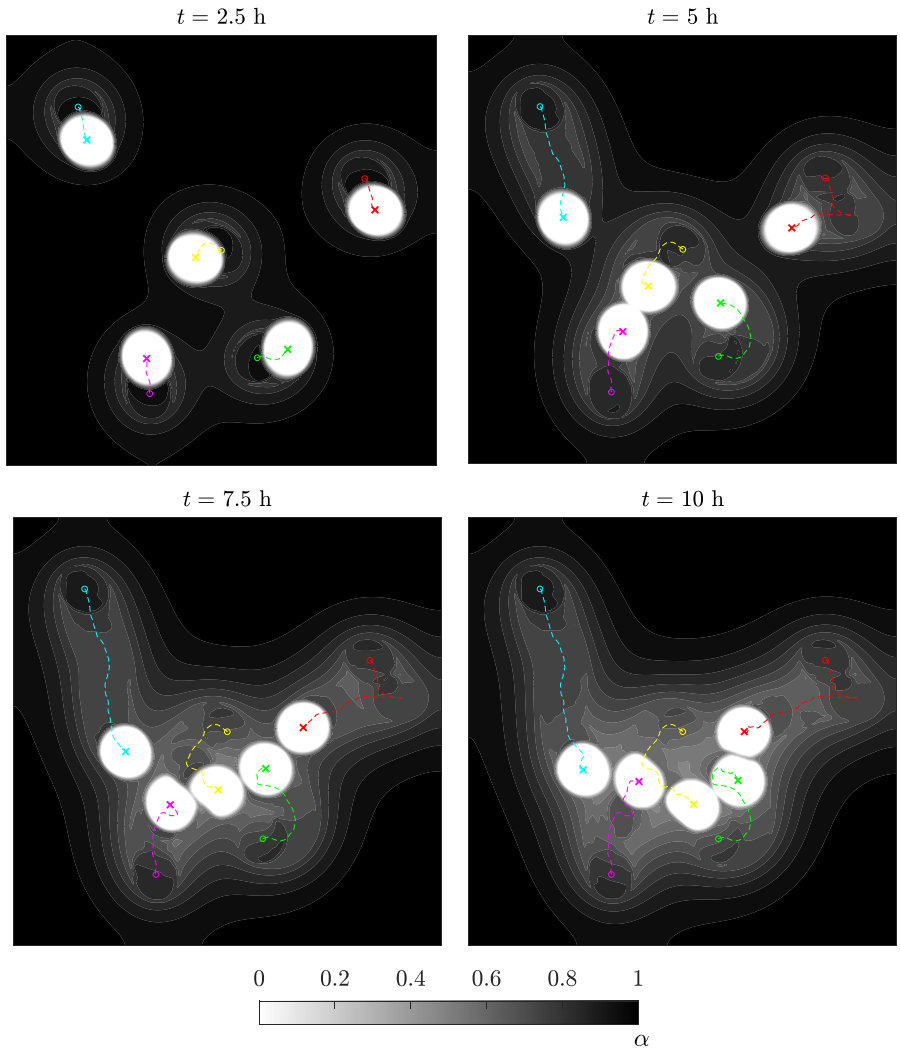


**Fig. 3** Map contours of the hydrogel crosslink density at four different times. White-colored regions, corresponding to $\alpha \simeq 0$, identify the space regions instantly occupied by the cells. The initial and current centroid positions of each cell are marked by a circle and a cross, respectively. The paths followed by the centroid of each cell up to the corresponding time are traced with differently colored dashed lines

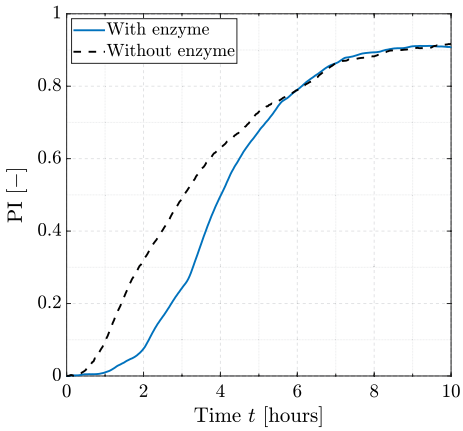


**Fig. 4** Packing Index curve over time for the current case study (solid blue line) compared to results obtained from our previous study [24] (dashed black line)

exhibits a continuous monotonic increment throughout the entire simulated time interval, with the exception of the initial minutes. In fact, in the early stage of the simulation, the excessively tight hydrogel network still hinders cell motion. The ultimate achieved PI value approximates unity ($\simeq 0.90$), confirming that a cluster characterized by quite densely packed cells has been formed. It is noteworthy that the derivative of PI with respect to time may be intended as a metric of the efficacy of cells' motion towards their compaction into a cluster, i.e. a positive (negative, respectively) slope of the PI curve indicates cells that are approaching (moving away, resp.) one other. As such, this depends on both the instantaneous relative polarization between cells, and the local enzyme concentration. The higher the enzyme concentration, the faster

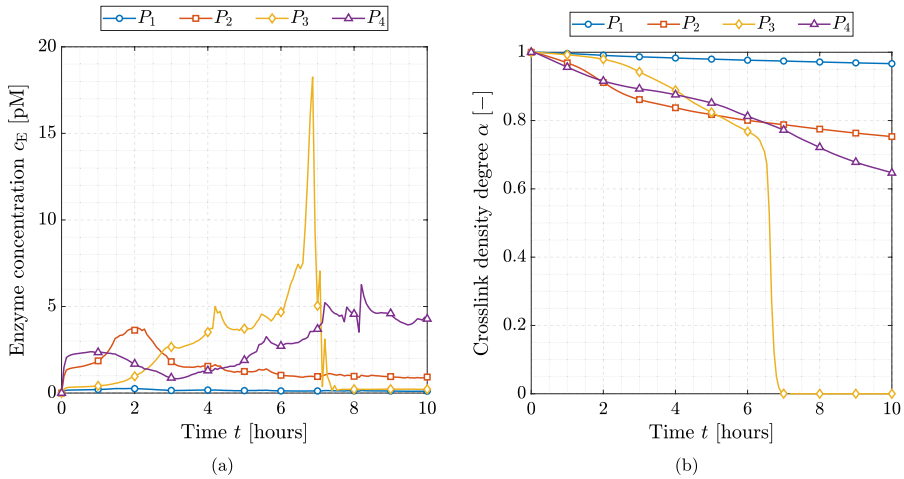


**Fig. 5** Plots of the enzyme total concentration (**a**) and the hydrogel crosslink density degree (**b**) at the material points $P_1$, $P_2$ $P_3$, $P_4$ introduced in Fig. 2

is the degradation and consequently cell motion. The PI obtained in the present case study suggest that, within a 8-hour interval, cells are effectively moving toward each other. Subsequently, the PI stabilizes, which is indicative of the formation of a cluster. In this regime, cells only exhibit a sliding relative motion in the cluster. Note also that, as mentioned in the foregoing, the incorporation of enzymatic degradation in the model slightly changes the average slope of the PI curve, and hence the average formation time of cellular clusters.

To gain deeper insights in the enzyme-induced spatio-temporal degradation of the hydrogel, we report in Fig. 5 plots of the variations over time in the total enzyme concentration $c_E$ and the hydrogel crosslink density at the four random probe points $P_1$, $P_2$, $P_3$, $P_4$ listed in Table 1 and shown in Fig. 2. Plots in Fig. 5 shed light on the considerable temporal and spatial variability in the hydrogel crosslink density, locally arising due to different total enzyme concentrations. Specifically, more rapid degradation kinetics of the hydrogel occurs as a consequence of higher total enzyme concentration. This can be clearly seen by comparing Figs. 5a and 5b, since steeper slopes of the plots in Fig. 5b are detected when the values of total enzyme concentration increases. For instance, point $P_1$ exhibits just a minor modification over time of the crosslink density, as confirmed by the scarcity of the enzyme therein present during all the analyzed timespan. Meanwhile, a quick increasing in the enzyme concentration is experienced around 6 h at position $P_3$, clear indication of a cell approaching at that location. In fact, the peak in enzyme concentration at point $P_3$ (attained at $t \simeq 6\,\mathrm{h}$) is followed by a time interval in which both the enzyme concentration and crosslink density degree vanish. This occurrence indicates that the position $P_3$ will be occupied by a cell for $t > 7\,\mathrm{h}$, since enzyme can only diffuse through the extracellular environment.

## 4 Conclusions and outlooks

In this paper, we have presented a computational strategy to model and improve the understanding of cell motion in polymeric environments that are sensitive to enzymes secreted by cells, enhancing the model already presented in [24]. Specifically, cells express enzymatic substances that cleave the hydrogel crosslinks, leading to a degradation dynamics of the polymer that significantly varies in both time and space, according to the local total enzyme concentration. By considering enzymatic rather than natural crosslink degradation in the hydrogel, the present approach offers a more detailed analysis of the chemo-biological mechanisms driving cell motion in polymeric environments. Indeed, although the trend of the Packing Index obtained in the present scenario is similar to that of our previous work, it exhibits a slightly delay in key events such as the initial time instant at which cells starts moving, and cell speed. Consequently, our current model allows to couple the dynamics of enzymes production and action with the one of cell clustering, extending the range of chemo-mechano-biological effects that can be explored with respect to our previous model.

Even if preliminary, obtained results align well with experimental evidence available in the literature, particularly regarding the average cellular clusters formation time [45]. Moreover, the model correctly captures the coupling between the main chemo-mechano-biological mechanisms characterizing cell motion and the spatio-temporal variations in the scaffolds chemo-physical properties.

While the model well reproduces the qualitative aspects of the process, some limitations still have to be faced. One aspect is that mechanical cues have only been incorporated in the model through high-stiffness barriers induced by the outer shell of the construct. Therefore, future work will be devoted to enhance the description of mechanical interactions between cells and the surrounding hydrogel, possibly by incorporating chemo-viscoelastic constitutive models for both cells and polymer scaffold in the modeling framework. Moreover, consideration for three-dimensional applications and a higher number of cells should be taken into account. Optimization of the process of neo-tissue formation in these scenarios is more challenging, as the proposed approach might not be computationally efficient due to the long simulation times. Finally, for a more detailed representation of the phenomenon, it may be beneficial to include other relevant cellular chemo-biological phenomena, such as cellular growth/replication and apoptosis. Nonetheless, despite the previous limitations, this paper demonstrates that our model has the potential to represent a valid support for the development of refined hybrid in vitro-in silico tools aimed at optimizing the process of neo-tissue formation in enzyme-degradable hydrogel scaffolds.

**Funding** Open access funding provided by Università degli Studi di Roma Tor Vergata within the CRUI-CARE Agreement. Part of this work was carried out with the support from the Italian National Group for Mathematical Physics GNFM-INdAM. The Authors acknowledge financial support by Regione Lazio (POR FESR LAZIO 2014; Progetti di Gruppi di Ricerca 2020; project: BIOPMEAT, n. A0375-2020-36756), as well as by the Italian Ministry of University and Research (MUR) under the National Recovery and Resilience Plan (NRRP), PRIN 2022 program, Project 2022T3SLAZ – CUP E53D23003700006.

**Data Availability** Data will be made available on request.

**Declarations**

**Conflict of interest** Pierfrancesco Gaziano and Michele Marino disclose any financial and personal relationships with other people or organizations that could inappropriately influence (bias) their work.

**Ethical approval** Not applicable.

## Appendix A Implementation details

In this section some additional details needed for the numerical implementation of the proposed modeling framework are reported. For the sake of notation, variables at the previous time step are denoted with the superscript $(n)$, while for the current time step the superscript is dropped out. Moreover, let $\Delta t$, $\Sigma = \partial\Omega_0$ and $\mathbf{n}_\Sigma$ be the current time increment, the boundary of the fixed computational domain, and the outward-pointing normal unit vector to $\Sigma$, respectively. Hence, for any admissible variations $\delta c_\mathrm{N}$, $\delta c_{\mathrm{S},j}$ ($\mathrm{S} \in \{\mathrm{A},\mathrm{E}\}$) and $\delta\phi_j$ (with $j = 1, \dots, C$) of the nodal variables, the weak form of the time-discretized version of Eqs. (8), (9) and (11) reads as:

$$\begin{aligned}
&\int_{\Omega_0} \frac{c_\mathrm{N} - c_\mathrm{N}^{(n)}}{\Delta t}\, \delta c_\mathrm{N}\, d\Omega + \int_{\Omega_0} \phi R_\mathrm{MM}\, \delta c_\mathrm{N}\, d\Omega \\
&\quad + \int_{\Omega_0} \nabla c_\mathrm{N} \cdot \nabla(D_\mathrm{N} \delta c_\mathrm{N})\, d\Omega \\
&\quad - int_\Sigma D_\mathrm{N} \nabla c_\mathrm{N} \cdot \mathbf{n}_\Sigma\, \delta c_\mathrm{N}\, d\Sigma = 0
\end{aligned} \tag{28}$$

$$\begin{aligned}
&\int_{\Omega_0} \frac{c_{\mathrm{S},j} - c_{\mathrm{S},j}^{(n)}}{\Delta t}\, \delta c_{\mathrm{S},j}\, d\Omega \\
&\quad - \int_{\Omega_0} \phi_{\mathrm{M},j} P_{\mathrm{S},j}\, \delta c_{\mathrm{S},j}\, d\Omega - \int_{\Omega_0} Q_{\mathrm{S},j}\, \delta c_{\mathrm{S},j}\, d\Omega \\
&\quad + \int_{\Omega_0} \nabla c_{\mathrm{S},j} \cdot \nabla(D_\mathrm{S} \delta c_{\mathrm{S},j})\, d\Omega \\
&\quad - \int_\Sigma D_\mathrm{S} \nabla c_{\mathrm{S},j} \cdot \mathbf{n}_\Sigma\, \delta c_{\mathrm{S},j}\, d\Sigma = 0
\end{aligned} \tag{29}$$

$$\int_{\Omega_0} \frac{\phi_j - \phi_j^{(n)}}{\Delta t}\,\delta\phi_j\,d\Omega + \int_{\Omega_0} \mathbf{v}_j \cdot \nabla\phi_j\,\delta\phi_j\,d\Omega + \int_{\Omega_0} \frac{\gamma}{\eta\varepsilon^2} G'(\phi_j)\,\delta\phi_j\,d\Omega + \int_{\Omega_0} \frac{\kappa}{\eta\varepsilon}\left(\frac{|\Omega_{\mathcal{C},j}(0)|}{|\Omega_0|} - \phi_j\right)\delta\phi_j\,d\Omega + \int_{\Omega_0} \frac{\gamma}{\eta}\nabla\phi_j \cdot \nabla(\delta\phi_j)\,d\Omega + \int_{\Omega_0} \frac{\zeta}{\eta\varepsilon}\sum_{h\neq j}^{N_C} \phi_h^2\phi_j d\Omega + \int_{\Omega_0} \frac{\sigma\varepsilon^2}{2\eta}\sum_{h\neq j}^{N_C} \left\|\nabla\phi_h\right\|^2 \nabla\phi_j \cdot \nabla(\delta\phi_j) d\Omega + \int_{\Sigma} \frac{\sigma\varepsilon^2}{2\eta}\sum_{h\neq j}^{N_C} \left\|\nabla\phi_h\right\|^2 \nabla\phi_j \cdot \mathbf{n}_\Sigma\,\delta\phi_j\,d\Sigma + \int_{\Sigma} \frac{\gamma}{\eta}\nabla\phi_j \cdot \mathbf{n}_\Sigma\,\delta\phi_j\,d\Sigma = 0. \tag{30}$$

As stated in Sect. 2.3, the discretized algebraic equation set associated to the above weak form, can be obtained by imposing the stationarity of the following pseudo-potential $\Pi$ function of the nodal variables $\mathbf{p}$:

$$\Pi = \int_{\Omega_0} \left(\Pi_N + \sum_{j=1}^{N_C} \left(\Pi_{A,j} + \Pi_{E,j} + \Pi_{\phi,j}\right)\right) d\Omega + \text{B.T.}, \tag{31}$$

where B.T. collects boundary terms associated to nutrient, enzyme and chemoattractant fluxes, and the contributions to the pseudo-potential related to the nutrient ($\Pi_N$), PF variables ($\Pi_{\phi,j}$), chemoattractant ($\Pi_{A,j}$) and enzyme ($\Pi_{E,j}$) are given by (S $\in$ {A,E}):

$$\Pi_N = b'_N\,c_N + \mathbf{b}''_N \cdot \nabla c_N \tag{32}$$

$$\Pi_{S,j} = b'_{S,j}\,c_{S,j} + \mathbf{b}''_{S,j} \cdot \nabla c_{S,j}, \tag{33}$$

$$\Pi_{\phi,j} = b'_{\phi,j}\,\phi_j + b''_{\phi,j}\left\|\nabla\phi_j\right\|^2 + b'''_{\phi,j}\phi_j, \tag{34}$$

where:

$$b'_N = \frac{c_N - c_N^{(n)}}{\Delta t} + \phi R_{MM}^{(n)} \tag{35}$$

$$\mathbf{b}''_N = \frac{1}{2} D_N \nabla c_N \tag{36}$$

$$b'_{S,j} = \frac{c_{S,j} - c_{S,j}^{(n)}}{\Delta t} - \phi_{M,j}^{(n)} P_{S,j} - Q_{S,j} \tag{37}$$

$$\mathbf{b}''_{S,j} = \frac{1}{2} D_S \nabla c_{S,j} \tag{38}$$

$$b'_{\phi,j} = \frac{\phi_j - \phi_j^{(n)}}{\Delta t} + \mathbf{v}_j \cdot \nabla\phi_j + \frac{\gamma}{\eta\varepsilon^2} G'(\phi_j) \tag{39}$$

$$b''_{\phi,j} = \frac{\gamma}{2\eta} - \frac{\sigma\varepsilon^2}{4\eta}\sum_{h\neq j}^{N_C} \left\|\nabla\phi_h\right\|^2 \tag{40}$$

$$b'''_{\phi,j} = \frac{\kappa}{\eta\varepsilon}\left(\frac{|\Omega_{\mathcal{C},j}(0)|}{|\Omega_0|} - \phi_j\right) + \frac{\zeta}{\eta\varepsilon}\sum_{h\neq j}^{N_C} \phi_h^2\phi_j. \tag{41}$$

Having defined the pseudo-potential $\Pi(\mathbf{p})$, the residual vector and the tangent matrix are derived as illustrated in Sect. 2.3, where the vector $\mathbf{B}$ to be held constant in Eq. (23) is the collection of all quantities appearing in Eqs. (35)-(41) for $j = 1, \ldots, N_C$.

## References


1. Groll J, Boland T, Blunk T, Burdick JA, Cho D-W, Dalton PD, Derby B, Forgacs G, Li Q, Mironov VA et al (2016) Biofabrication: reappraising the definition of an evolving field. Biofabrication 8(1):013001
2. Berthiaume F, Maguire TJ, Yarmush ML (2011) Tissue engineering and regenerative medicine: history, progress, and challenges. Annu Rev Chem Biomol Eng 2:403–430
3. Post MJ, Levenberg S, Kaplan DL, Genovese N, Fu J, Bryant CJ, Negowetti N, Verzijden K, Moutsatsou P (2020) Scientific, sustainability and regulatory challenges of cultured meat. Nature Food 1(7):403–415
4. Khademhosseini A, Langer R (2016) A decade of progress in tissue engineering. Nat Protoc 11(10):1775–1781
5. Shukla PR, Skeg J, Buendia EC, Masson-Delmotte V, Pörtner H-O, Roberts D, Zhai P, Slade R, Connors S, Van Diemen S, et al (2019) Climate change and land: an IPCC special report on climate change, desertification, land degradation, sustainable land management, food security, and greenhouse gas fluxes in terrestrial ecosystems
6. Malda J, Visser J, Melchels FP, Jüngst T, Hennink WE, Dhert WJ, Groll J, Hutmacher DW (2013) 25th anniversary article: engineering hydrogels for biofabrication. Adv Mater 25(36):5011–5028
7. Zhu J, Marchant RE (2011) Design properties of hydrogel tissue-engineering scaffolds. Expert Rev Med Devices 8(5):607–626
8. Seliktar D (2012) Designing cell-compatible hydrogels for biomedical applications. Science 336(6085):1124–1128
9. Dikovsky D, Bianco-Peled H, Seliktar D (2006) The effect of structural alterations of PEG-fibrinogen hydrogel scaffolds on 3-D cellular morphology and cellular migration. Biomaterials 27(8):1496–1506
10. Sridhar BV, Brock JL, Silver JS, Leight JL, Randolph MA, Anseth KS (2015) Development of a cellularly degradable peg hydrogel to promote articular cartilage extracellular matrix deposition. Adv Healthcare Mater 4(5):702–713
11. Bryant SJ, Anseth KS (2002) Hydrogel properties influence ecm production by chondrocytes photoencapsulated in poly (ethylene glycol) hydrogels. J Biomed Mater Res 59(1):63–72
12. Bahney CS, Hsu C-W, Yoo JU, West JL, Johnstone B (2011) A bioresponsive hydrogel tuned to chondrogenesis of human mesenchymal stem cells. FASEB J 25(5):1486
13. Chu S, Sridhar SL, Akalp U, Skaalure SC, Vernerey FJ, Bryant SJ (2017) Understanding the spatiotemporal degradation behavior of aggrecanase-sensitive poly (ethylene glycol) hydrogels for use in cartilage tissue engineering. Tissue Eng Part A 23(15–16):795–810
14. Akalp U, Bryant SJ, Vernerey FJ (2016) Tuning tissue growth with scaffold degradation in enzyme-sensitive hydrogels: a mathematical model. Soft Matter 12(36):7505–7520
15. Liu J, Hilderink J, Groothuis TA, Otto C, Van Blitterswijk CA, Boer J (2015) Monitoring nutrient transport in tissue-engineered grafts. J Tissue Eng Regen Med 9(8):952–960
16. Campos D, Méndez V, Llopis I (2010) Persistent random motion: Uncovering cell migration dynamics. J Theor Biol 267(4):526–534
17. Camley BA, Rappel W-J (2017) Physical models of collective cell motility: from cell to tissue. J Phys D Appl Phys 50(11):113002
18. Mak M, Spill F, Kamm RD, Zaman MH (2016) Single-cell migration in complex microenvironments: mechanics and signaling dynamics. J Biomech Eng 138(2):021004
19. Lo C-M, Wang H-B, Dembo M, Wang Y-L (2000) Cell movement is guided by the rigidity of the substrate. Biophys J 79(1):144–152
20. Conti M, Santesarti G, Scocozza F, Marino M (2022) Models and simulations as enabling technologies for bioprinting process design. In: Bioprinting, pp. 137–206. Academic Press: Cambridge
21. Vis MA, Ito K, Hofmann S (2020) Impact of culture medium on cellular interactions in in vitro co-culture systems. Fronti Bioeng Biotechnol 8:911
22. Möller J, Pörtner R, Gowder S (2017) New insights into cell culture technology. InTech, London
23. Hardman D, Hennig K, Gomes E, Roman W, Bernabeu MO (2021) An in vitro-agent based modelling approach to optimisation of culture medium for generating muscle cells. bioRxiv
24. Gaziano P, Marino M (2023) A phase-field model of cell motility in biodegradable hydrogel scaffolds for tissue engineering applications. Computational Mechanics, 1–22
25. Almany L, Seliktar D (2005) Biosynthetic hydrogel scaffolds made from fibrinogen and polyethylene glycol for 3D cell cultures. Biomaterials 26(15):2467–2477
26. Moure A, Gomez H (2021) Phase-field modeling of individual and collective cell migration. Arch Comput Methods Eng 28(2):311–344
27. Nonomura M (2012) Study on multicellular systems using a phase field model. PLoS ONE 7(4):33501
28. Camley BA, Zhang Y, Zhao Y, Li B, Ben-Jacob E, Levine H, Rappel W-J (2014) Polarity mechanisms such as contact inhibition of locomotion regulate persistent rotational motion of mammalian cells on micropatterns. Proc Natl Acad Sci 111(41):14770–14775
29. Korelc J, Wriggers P (2016) Automation of finite element methods. Springer, New York
30. Kreft M, Lukšič M, Zorec TM, Prebil M, Zorec R (2013) Diffusion of D-glucose measured in the cytosol of a single astrocyte. Cell Mol Life Sci 70(8):1483–1492
31. Gu WY, Yao H, Vega AL, Flagler D (2004) Diffusivity of ions in agarose gels and intervertebral disc: effect of porosity. Ann Biomed Eng 32(12):1710–1717
32. Oliveira L, Carvalho MI, Nogueira E, Tuchin VV (2013) The characteristic time of glucose diffusion measured for muscle tissue at optical clearing. Laser Phys 23(7):075606
33. Mookerjee SA, Gerencser AA, Nicholls DG, Brand MD (2017) Quantifying intracellular rates of glycolytic and oxidative ATP production and consumption using extracellular flux measurements. J Biol Chem 292(17):7189–7207
34. Olson SD, Haider MA (2019) A computational reaction-diffusion model for biosynthesis and linking of cartilage extracellular matrix in cell-seeded scaffolds with varying porosity. Biomech Model Mechanobiol 18(3):701–716
35. Obradovic B, Meldon JH, Freed LE, Vunjak-Novakovic G (2000) Glycosaminoglycan deposition in engineered

cartilage: experiments and mathematical model. AIChE J 46(9):1860–1871
36. Cruise GM, Scharp DS, Hubbell JA (1998) Characterization of permeability and network structure of interfacially photopolymerized poly(ethylene glycol) diacrylate hydrogels. Biomaterials 19(14):1287–1294
37. Yu S, Duan Y, Zuo X, Chen X, Mao Z, Gao C (2018) Mediating the invasion of smooth muscle cells into a cell-responsive hydrogel under the existence of immune cells. Biomaterials 180:193–205
38. Ebata H, Yamamoto A, Tsuji Y, Sasaki S, Moriyama K, Kuboki T, Kidoaki S (2018) Persistent random deformation model of cells crawling on a gel surface. Sci Rep 8(1):1–12
39. Tibbitt MW, Kloxin AM, Sawicki LA, Anseth KS (2013) Mechanical properties and degradation of chain and step-polymerized photodegradable hydrogels. Macromolecules 46(7):2785–2792
40. Bausch AR, Ziemann F, Boulbitch AA, Jacobson K, Sackmann E (1998) Local measurements of viscoelastic parameters of adherent cell surfaces by magnetic bead microrheometry. Biophys J 75(4):2038–2049
41. Shao D, Rappel W-J, Levine H (2010) Computational model for cell morphodynamics. Phys Rev Lett 105(10):108104
42. McLennan R, Dyson L, Prather KW, Morrison JA, Baker RE, Maini PK, Kulesa PM (2012) Multiscale mechanisms of cell migration during development: theory and experiment. Development 139(16):2935–2944
43. Costantini M, Testa S, Fornetti E, Fuoco C, Sanchez Riera C, Nie M, Bernardini S, Rainer A, Baldi J, Zoccali C et al (2021) Biofabricating murine and human myo-substitutes for rapid volumetric muscle loss restoration. EMBO Mol Med 13(3):12778
44. Ostrovidov S, Hosseini V, Ahadian S, Fujie T, Parthiban SP, Ramalingam M, Bae H, Kaji H, Khademhosseini A (2014) Skeletal muscle tissue engineering: methods to form skeletal myotubes and their applications. Tissue Eng Part B Rev 20(5):403–436
45. Eigler T, Zarfati G, Amzallag E, Sinha S, Segev N, Zabary Y, Zaritsky A, Shakked A, Umansky K-B, Schejter ED et al (2021) Erk1/2 inhibition promotes robust myotube growth via camkii activation resulting in myoblast-to-myotube fusion. Dev Cell 56(24):3349–3363